Novel Lithium Iron Pyrophosphate ($LiFe_{1.5}P_2O_7$) as a Positive Electrode for Li-Ion Batteries

C. V. Ramana,*,† A. Ait-Salah,‡ S. Utsunomiya,† A. Mauger,§ F. Gendron,‡ and C. M. Julien‡

Nanoscience and Surface Chemistry Laboratory, Department of Geological Sciences, University of Michigan, Ann Arbor, Michigan 48109, Institut des Nano-Sciences de Paris, Université Pierre et Marie Curie, CNRS-UMR 7588, and Institut de Minéralogie et Physique de la Matière Condensée, Université Pierre et Marie Curie, CNRS-UMR 7590, campus Boucicaut, 140 rue de Lourmel, 75015 Paris, France

Received June 7, 2007. Revised Manuscript Received August 6, 2007

Lithium iron pyrophosphate ($LiFe_{1.5}P_2O_7$) has been synthesized by a wet-chemical method for application in lithium-ion batteries. Structural analysis using X-ray diffraction and high-resolution electron microscopy indicate that $LiFe_{1.5}P_2O_7$ synthesized at 500 °C, using metal acetates, is crystallized in the monoclinic structure with lattice parameters $a = 0.698\ 76$ nm, $b = 0.812\ 36$ nm, $c = 0.964\ 22$ nm, and $\beta = 111.83°$ ($P2_1/c$ space group). Electrochemical characterization of $LiFe_{1.5}P_2O_7$ in lithium cells indicates a capacity of 95 mA·h/g obtained in the voltage range 2.5−4.2 V. The resulting incremental capacity indicates a stable structure for the first cycle with the redox peaks at 3.33 and 3.22 V versus Li^0/Li^+. The capacity of $LiFe_{1.5}P_2O_7$ decreased with cycling number at the rate of 0.22% per cycle while the capacity falls off rapidly in the case of material prepared at higher temperatures.

I. Introduction

Lithium iron phosphates form an important group of ceramic compounds that are now being investigated extensively as prospective positive electrode materials for rechargeable lithium-ion batteries.[1−20] Requirements in the development of rechargeable lithium-ion batteries demand suitable active electrode materials that can exhibit high potential versus Li^+/Li^0, good charge/discharge cycleability, and high thermal stability. Among the phosphate group materials, the phospho-olivine $LiFePO_4$ was the first to be proposed and demonstrated as a lithium intercalation electrode by Padhi et al.[1] Currently, there has been a great deal of interest to identify new phosphate materials built by polyanions such as $(PO_4)^{3-}$, $(P_2O_7)^{4-}$, or $(P_3O_{10})^{5-}$ and exhibiting enhanced thermal stability that improves safety of lithium cells at high temperature (60 °C). One of the key aspects of this class of materials is the major structural anomalies, such as anisotropic deformation, significant loss

† University of Michigan.
‡ Institut des Nano-Sciences de Paris, Université Pierre et Marie Curie.
§ Institut de Minéralogie et Physique de la Matière Condensée, Université Pierre et Marie Curie.

(1) Padhi, A. K.; Nanjundaswamy, K. S.; Goodenough, J. B. *J. Electrochem. Soc.* **1997**, *144*, 1188.
(2) (a) Chen, G.; Song, X.; Richardson, T. J. *J. Electrochem. Soc.* **2007**, *154*, A627. (b) Chen, G.; Song, X.; Richardson, T. J. *Electrochem. Solid-State Lett.* **2006**, *9*, A295.
(3) Yamada, A.; Koizumi, H.; Nishimura, S.-I.; Sonoyama, N.; Kanno, R.; Yonemura, Y.; Nakamura, T.; Kobayashi, Y. *Nat. Mater.* **2006**, *5*, 357.
(4) Allen, J. L.; Jow, T. R.; Wolfenstine, J. *Chem. Mater.* **2007**, *19*, 2108.
(5) Park, K. S.; Schougaard, S. B.; Goodenough, J. B. *Adv. Mater.* **2007**, *19*, 848.
(6) Srinivasan, V.; Newmann, J. *Electrochem. Solid-State Lett.* **2006**, *9*, A110.
(7) (a) Herle, P. S.; Ellis, B.; Coombs, N.; Nazar, L. F. *Nat. Mater.* **2004**, *3*, 147. (b) Huang, H.; Yin, S.-C.; Nazar, L. F. *Electrochem. Solid-State Lett.* **2001**, *4*, A170.
(8) (a) Ait-Salah, A.; Mauger, A.; Julien, C. M.; Gendron, F. *Mater. Sci. Eng. B* **2006**, *129*, 232. (b) Ait-Salah, A.; Mauger, A.; Zaghib, K.; Goodenough, J. B.; Ravet, N.; Gauthier, M.; Gendron, F.; Julien, C. M. *J. Electrochem. Soc.* **2006**, *153*, A1692. (c) Ait-Salah, A.; Jozwiak, P.; Garbarczyk, J.; Benkhouja, K.; Zaghib, K.; Gendron, F.; Julien, C. M. *J. Power Sources* **2005**, *140*, 370.
(9) (a) Morgan, D.; Ven, A. V. D.; Ceder, G.; *Electrochem. Solid-State Lett.* **2004**, *7*, A30. (b) Maxisch, T.; Zhou, F.; Ceder, G. *Phys. Rev. B* **2006**, *73*, 104301. (c) Zhou, F.; Maxisch, T.; Ceder, G. *Phys. Rev. Lett.* **2006**, *97*, 155704.
(10) (a) Ramana, C. V.; Ait-Salah, A.; Utsunomiya, S.; Morhange, J.-F.; Mauger, A.; Gendron, F.; Julien, C. M. *J. Phys. Chem. C* **2007**, *111*, 1049. (b) Ramana, C. V.; Ait-Salah, A.; Julien, C. M. *Mater. Sci. Eng. B* **2007**, *135*, 78.
(11) Islam, S. M.; Driscoll, D. J.; Fisher, C. A. J.; Slater, P. R.; *Chem. Mater.* **2005**, *17*, 5085.
(12) (a) Zaghib, K.; Striebel, K. A.; Guerfi, A.; Shim, J.; Armand, M.; Gauthier, M. *Electrochim. Acta* **2004**, *50*, 263. (b) Wang, C. W.; Sastry, A. M.; Striebel, K. A.; Zaghib, K. *J. Electrochem. Soc.* **2005**, *152*, A1001. (c) Zaghib, K.; Ravet, N.; Gauthier, M.; Goodenough, J. B.; Mauger, A.; Gendron, F.; Julien, C. M. *J. Power Sources* **2006**, *163*, 560. (d) Guerfi, A.; Kaneko, M.; Petitclerc, M.; Mori, M.; Zaghib, K. *J. Power Sources* **2007**, *163*, 1047.
(13) (a) Ravet, N.; Chouinard, Y.; Magnan, J.-F.; Besner, S.; Gauthier, M.; Armand, M. *J. Power Sources* **2001**, *97*−*98*, 503. (b) Ravet, N.; Abouimrane, A.; Armand, M. *Nat. Mater.* **2003**, *2*, 702. (c) Ravet, N.; Gauthier, M.; Zaghib, K.; Goodenough, J. B.; Mauger, A.; Gendron, F.; Julien, C. M. *Chem. Mater.* **2007**, *19*, 2595.
(14) (a) Dodd, J. L.; Yazami, R,; Fultz, B. *Electrochem. Solid-State Lett.* **2006**, *9*, A151. (b) Dodd, J. L.; Halevy, I.; Fultz, B. *J. Phys. Chem. C* **2007**, *111*, 1563. (c) Stevens, R.; Dodd, J. L.; Kresch, M. G.; Yazami, R.; Fultz, B.; Ellis, B.; Nazar, L. F. *J. Phys. Chem. B* **2006**, *110*, 22732.
(15) Tucker, M. C.; Doeff, M. M.; Richardson, T. J.; Finones, R.; Cairns, E. J.; Reimer, J. A. *J. Am. Chem. Soc.* **2002**, *124*, 3832.
(16) Giorgetti, M.; Berrettoni, M.; Scaccia, S.; Passerini, S. *Inorg. Chem.* **2006**, *45*, 2750.
(17) (a) Whittingham, M. S. *Chem. Rev.* **2004**, *104*, 4271. (b) Yang, S.; Zavalij, P. Y.; Whittingham, M. S. *Electrochem. Commun.* **2001**, *3*, 505. (c) Chen, J. J.; Whittingham, M. S. *Electrochem. Commun.* **2006**, *8*, 855.
(18) Julien, C. M.; Zaghib, K.; Mauger, A.; Massot, M.; Ait-Salah, A.; Selmane, M.; Gendron, F. *J. Appl. Phys.* **2006**, *100*, 063511.
(19) Hsu, K. F.; Tsay, S. Y.; Hwang, B. J. *J. Mater. Chem.* **2004**, *14*, 2690.
(20) Paraguassu, W.; Freire, P. T. C.; Lemos, V.; Lala, S. M.; Montoro, L. A.; Rosolen, J. M. *J. Raman Spectrosc.* **2005**, *36*, 213.

10.1021/cm071526m CCC: $37.00
Published on Web 10/09/2007

of long-range order, local phase segregation, and clustering impurities, strongly depend on the preparation conditions.[3,8,10] Another interesting feature is the low valence configuration of the transition metal (M) in the electrode material in the discharged state, that is, Fe^{2+} for iron ions that allows oxidation at potential higher than 3 V versus Li^+/Li^0. The dilithium tri-iron bi(diphosphate) $Li_2Fe_3(P_2O_7)_2$ (named hereafter $LiFe_{1.5}P_2O_7$) could be a candidate as a positive electrode material for Li-ion batteries providing a theoretical capacity of 101 mA·h/g when one electron is transferred. The structural type of these ABP_2O_7 mixed phosphate compounds depends on the size of the A and B cations and the conformation of the $(P_2O_7)^{4-}$ oxo-anions. Prototype pyrophosphate frameworks with the thortveitite-like structure (with staggered P_2O_7 groups) are α-$Ni_2P_2O_7$ and $Mg_2P_2O_7$.[21,22] Depending of the cation size there are three types of structure including cage, sheet, or tunnel framework.[23−25] However, compounds can crystallize with the partial substitution of an alkali metal (lithium) for a transition-metal element, but these materials are rarely mentioned in the literature. Rissouli et al.[26−28] have reported the structural and magnetic properties of $LiM_{1.5}P_2O_7$ (M = Ni, Co, Cu), but no data are available for $LiFe_{1.5}P_2O_7$ so far.

The emphasis in this work is on the wet-chemical synthesis using metal acetates and characterization of $LiFe_{1.5}P_2O_7$ for application in lithium-ion batteries as a positive electrode. An understanding of the structural features and the morphology is of crucial importance for new electrode materials. Improved understanding of the structure on the reduced dimensionality is highly desired not only for integrating these materials into technological applications but also for the fundamental reason that the growth, crystal structure, surface morphology, and chemical composition of the materials significantly affect their electrochemical performance.[12,13] In this context, we have made attempts to understand the physical, geometric, and chemical structure and electrochemical properties of as-grown $LiFe_{1.5}P_2O_7$. Using the results obtained on $LiFe_{1.5}P_2O_7$, we discuss the structural quality, chemical homogeneity, and application of the materials in lithium-ion battery technology.

II. Experimental Section

A. Synthesis. $LiFe_{1.5}P_2O_7$ samples were synthesized by a wet-chemical route at moderate temperatures. Lithium acetate dihydrate $Li(COOCH_3)\cdot 2H_2O$, iron acetate hydrate $Fe(COOCH_3)_2\cdot H_2O$, and phosphoric(V) acid H_3PO_4 (Fluka purum grade) were used as starting materials in this method. Raw materials were mixed in a molar ratio of Li/Fe/P = 1.05:1.5:2 in *N*,*N*-dimethylformamide with careful stirring for 24 h. Excess of lithium is needed to prevent loss of stoichiometry in the final product. The solvent was slowly evaporated at 120 °C in air. After a careful grinding, the solid dry residue was pre-heated at 350 °C for 2 h for the formation of the phosphate precursor. Successive grinding operations were performed before the final heat treatment in the temperature range of 500−600 °C for 24 h. The calcination procedures were carried out in a flow of Ar/H_2 gas (85:15) to prevent any oxidation of iron into Fe^{3+} ions. A gray fine powder was then obtained and characterized by various analytical techniques to check the purity of the resulting phase.

B. Characterization. The X-ray diffracton (XRD) patterns were recorded on a Philips X'Pert PRO MRD (PW3050) diffractometer equipped with a Cu anticathode (Cu Kα radiation $\lambda = 1.540\,56$ Å) at room temperature. The measurements were made under Bragg−Brentano geometry at a slow sweep by steps of $2\theta = 0.05°$ in the range of 10−80° to obtain the data for Rietveld refinement. The structure of $LiFe_{1.5}P_2O_7$ was determined by Rietveld refinement using the EXPGUI interface.[29] Transmission electron microscopy (TEM) analysis was performed using a Jeol TEM2010F at a 200 kV acceleration voltage. Phase and structure material were monitored using selected area electron diffraction (SAED). The chemical quality was analyzed by energy-dispersive X-ray spectroscopy (EDS) in the TEM column utilizing EDAX Genesis software. The specimen for TEM analysis was prepared by dispersing $LiFe_{1.5}P_2O_7$ on a 3-mm Cu grid with a hole size of 1 × 2 mm. High-resolution transmission electron microscopy (HRTEM) and elemental mapping were completed by high-angle annular dark field scanning transmission electron microscopy (HAADF-STEM) using Emispec ES Vision version 4.0 of the STEM-EDX mapping system. To minimize the effect of sample drift, a drift-correcting mode was used during the acquisition of EDS maps. The sample was carefully positioned in the TEM column, and the EDS spectra of $LiFe_{1.5}P_2O_7$ were recorded, with Cu grid as a reference, to avoid any additional contamination. The specifications of STEM are listed as follows: Cs is 1.0 mm, probe size is 0.5 nm for analysis and 0.2 for high-resolution imaging, the collection angle of the HAADF detector is 50−110 mrad, the objective aperture size is 30 μm for analysis and 20 μm for high-resolution imaging, and the defocus condition is approximately −55 nm. Image processing including the fast Fourier transformation (FFT) was carried out by Gatan Digital Micrograph 3.4.

C. Electrochemical Studies. The electrochemical properties of the product were tested at 25 °C in cells with metallic lithium as the negative electrode using Teflon laboratory-cell hardware and Mac-Pile system. The nonaqueous electrolyte was the DEC−EC mixture (1:1 in volume) containing 1.0 mol/dm^3 $LiPF_6$. The active electrode material was deposited onto Al foil at the loading of 8.7 mg/cm^2. The galvanostatic charge−discharge processes were carried out at the rate C/20 in the voltage range 2.5−4.2 V versus Li^0/Li^+.

III. Results And Discussion

A. Structure. The XRD pattern of $LiFe_{1.5}P_2O_7$ synthesized at 500 °C along with the calculated pattern using Rietveld refinement is shown in Figure 1. The XRD pattern indicates the formation of crystalline $LiFe_{1.5}P_2O_7$, which is a single phase and impurity-free material, with the absence of any other oxide phases. The XRD results also indicate that the grown $LiFe_{1.5}P_2O_7$ crystallizes in the thortveitite-like structure. Refinements of the XRD pattern using the monoclinic

(21) Lukaszewicz, K. *Bull. Acad. Pol. Sci. Chim*. **1967**, *15*, 47.
(22) Calvo, C. *Can. J. Chem*. **1965**, *43*, 1147.
(23) Riou, D.; Labbe, P.; Goreaud, M. *C.R. Acad. Sci. (Paris) C* **1988**, *307*, 903.
(24) Riou, D.; Leligny, H.; Pham, C.; Labbe, P.; Raveau, B. *Acta Crystallogr., Sect. B* **1991**, *47*, 608.
(25) Riou, D.; Raveau, B. *Acta Crystallogr., B* **1991**, *47*, 1708.
(26) Rissouli, K.; Benkhouja, K.; Sadel, A; Bettach, M.; Zahir, M.; Giorgi, M.; Pierrot, M. *Acta Crystallogr., Sect. C* **1996**, *52*, 2960.
(27) Rissouli, K.; Bettach, M.; Benkhouja, K.; Sadel, A.; Zahir, M.; Giorgi, M.; Pierrot, M.; Derrory, A.; Drillon, M. *Ann. Chem. Sci. Mater*. **1998**, *23*, 103.
(28) Rissouli, K.; Benkhouja, K.; Touaiher, M.; Sadel, A.; Aride, J.; Derrory, A.; Lambour, J. P.; Drillon, M. *Phys. Chem. News* **2001**, *2*, 119.
(29) Toby, B. H. J. *Appl. Crystallogr*. **2001**, *34*, 210.

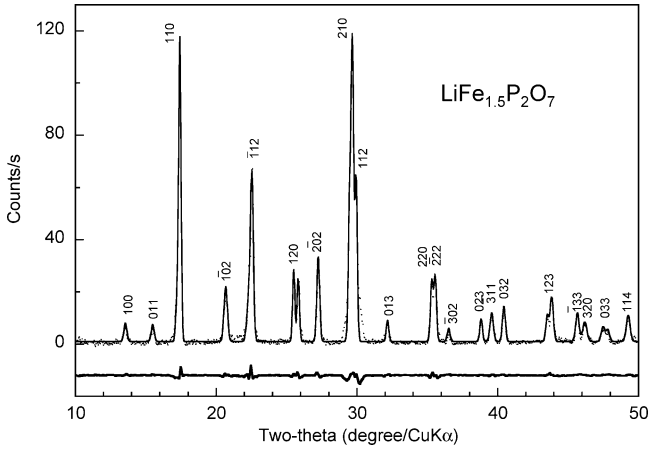

Figure 1. XRD pattern for LiFe$_{1.5}$P$_2$O$_7$ pyrophosphate powders synthesized by a solution route from metal acetate precursors. Cu Kα radiation was used. Experimental and calculated patterns and the difference are shown in the graph. The XRD lines are indexed in the monoclinic structure in the $P2_1/c$ space group. Rietveld refinement was obtained using the EXPGUI interface.[17]

Table 1. Refined Atom Positions for LiFe$_{1.5}$P$_2$O$_7$

atom	*x*/*a*	*y*/*b*	*z*/*c*	U_{ISO}
Li	−0.2910	0.0820	0.6345	3.59
Fe(1)	−0.1871	0.1268	0.9802	2.88
Fe(2)	0.000	0.000	0.000	2.65
P(1)	0.1178	0.2064	0.8051	2.91
P(2)	0.4051	−0.0512	0.7843	2.85
O(1)	0.3251	0.1348	0.8100	1.96
O(2)	0.0333	0.0788	0.8912	2.25
O(3)	−0.0086	0.2065	0.6361	2.78
O(4)	0.6171	−0.0098	0.8021	2.69
O(5)	0.3788	−0.1702	0.9038	2.51
O(6)	0.2777	−0.1133	0.6235	2.12
O(7)	0.1534	0.3781	0.8828	2.67

system ($P2_1/c$ space group) lead to the lattice parameters a = 0.698 76 nm, b = 0.812 36 nm, c = 0.964 22 nm, and β=111.83°. The atomic positions obtained after refinement are listed in Table 1. The small reliability factors (R_{wp} = 12.3% and R_B = 9.82%) and the good minimization of the difference $|I_{obsvd} - I_{calcd}|$ suggest a good description of the structure of the LiFe$_{1.5}$P$_2$O$_7$ sample. However, some of the diffracted intensity is not well modeled, in particular at the base of the (110) peak, between the ($\bar{1}02$) and the ($\bar{1}12$) peaks, as well as at the base of the (210)/(112) peaks that could be due to some impurities in the amorphous state. The estimated crystallite size, using the Scherrer's formula and width of the (110) peak, is ∼50 nm. The XRD pattern of LiFe$_{1.5}$P$_2$O$_7$ synthesized at 600 °C showed some extra peaks due to the formation of impurity phase such as iron phosphide.

The three-dimensional framework of LiFe$_{1.5}$P$_2$O$_7$ is built up from edge-sharing FeO_6 octahedra and P_2O_7 groups (Figure 2a). The crystal can be therefore formulated as ionic with $(Li_2Fe_3)^{8+}$ as the cation and $(P_2O_7)_2^{8-}$ as the anion. The P_2O_7 oxo-anion consists of two PO_4 tetrahedra sharing a bridging oxygen atom with a P−O−P angle of approximately 134° in the staggered configuration (Figure 2b). The Fe^{2+} ions occupy two types of nonequivalent octahedral sites and the edge-sharing FeO_6 octahedra that form trimer chains in a zigzag arrangement running parallel to the *b*-axis (Figure 2). The independent octahedral sites are of prime importance for the electrochemical properties because they could induce

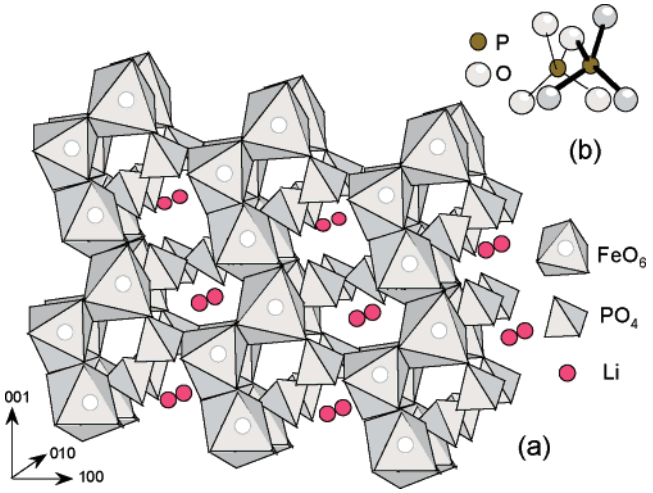

Figure 2. (a) Schematic representation of the pyrophosphate structure for LiFe$_{1.5}$P$_2$O$_7$. The three-dimensional framework of LiFe$_{1.5}$P$_2$O$_7$ is built up from edge-sharing FeO_6 octahedra and P_2O_7 groups forming tunnels within which the Li^+ ions are located. (b) View of the $(P_2O_7)^{4-}$ oxo-anion showing the staggered connectivity of PO_4 tetrahedra sharing corners.

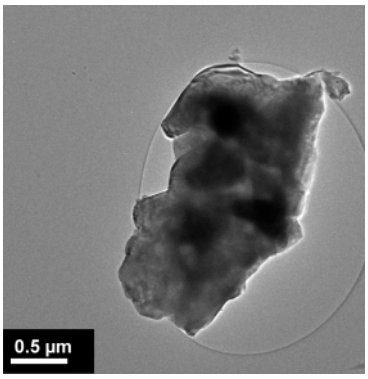

Figure 3. Bright-field TEM image of LiFe$_{1.5}$P$_2$O$_7$. The image shows the formation of microcrystalline particles.

steps in the discharge process. This structural aspect was also confirmed by the magnetic measurements discussed below. LiFe$_{1.5}$P$_2$O$_7$ appears to be isostructural with LiNi$_{1.5}$P$_2$O$_7$.[26] Its structure is related to that of α-$Ni_2P_2O_7$ by replacement of the five-coordinate M site by Li. The sequence of M^{2+} atoms in α-$Ni_2P_2O_7$ (two-dimensional configuration) is disrupted by Li^+ polyhedra to give rise to trimers formed of zigzag strips of FeO_6 octahedra (one-dimensional configuration) in LiFe$_{1.5}$P$_2$O$_7$.

The bright-field TEM image of LiFe$_{1.5}$P$_2$O$_7$ shown in Figure 3 indicates that the material contains microcrystalline particles, which was also confirmed by scanning electron microscopy (SEM; not shown) and XRD measurements. The agglomeration of crystalline particles of the material could be due to the intrinsic nature of the sample grown by the wet-chemical method. The particle surfaces exhibit smooth morphology. The features of the particles, in terms of size, shape, and distribution, observed in SEM and TEM are in good agreement. The HRTEM and SAED patterns of LiFe$_{1.5}$P$_2$O$_7$ are shown in Figure 4. The FFT of the selected region of the HRTEM image is also shown in the inset (Figure 4a). The lattice fringes in the HRTEM are due to crystalline LiFe$_{1.5}$P$_2$O$_7$. It is important to recognize that the lattice resolution using HRTEM of LiFe$_{1.5}$P$_2$O$_7$ does not reveal any lattice defects such as dislocations and misfits.

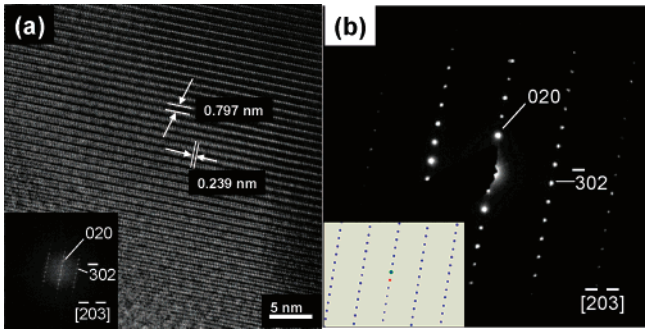

Figure 4. (a) HRTEM image $LiFe_{1.5}P_2O_7$. The well-resolved lattice fringes indicate the crystallinity of the sample. The measured values of lattice fringe spacing values in vertical and horizontal directions are as indicated. Inset on the left corner (bottom) shows the FFT of the HRTEM image, which indicates the direction in which the crystallite was examined and lattice planes contributing to the diffraction. (b) SAED patterns of $LiFe_{1.5}P_2O_7$. The assignment of diffraction maxima and the direction of view are indicated. Inset shows the diffraction pattern obtained by simulation using the TEM experimental parameters and lattice parameters obtained from XRD.

The lattice fringes are uniform and continuous without any terminating lines or misalignment or surface modulations, for several particles examined, which is a true indication of the structural quality of $LiFe_{1.5}P_2O_7$. The SAED pattern (Figure 4b), which was obtained in the same position as in HRTEM, indicates the diffraction maxima due to reflections from the ($\bar{3}02$) and (010) lattice planes of $LiFe_{1.5}P_2O_7$. The measured fringe spacing values are 0.239 nm (d_{010}) and 0.797 nm ($d_{\bar{3}02}$) in the in the horizontal and vertical directions, respectively. These experimental values are in agreement with the corresponding calculated values ($d_{\bar{3}02} = 0.810$ nm; $d_{010} = 0.237$ nm) using XRD data of $LiFe_{1.5}P_2O_7$. To further confirm the structure of the material, the diffraction pattern has been simulated, using an electron beam of 200 kV incident along the ($\bar{2}0\bar{3}$) direction for calculations, which is shown as an inset in Figure 4b. The simulated pattern is similar to the one obtained in the experiment, which indicates the validity of our assignment of lattice planes and monoclinic structure of $LiFe_{1.5}P_2O_7$. Thus the HRTEM, SAED, and XRD studies confirm the stable monoclinic $LiFe_{1.5}P_2O_7$ phase without any impurities or lattice defects.

The EDS spectrum and the HAADF-STEM elemental mapping images of $LiFe_{1.5}P_2O_7$ are shown in Figure 5. The EDS spectrum (Figure 5; upper panel) exhibits the characteristic peaks of Fe, P, and O present in the sample. It is not possible to detect Li for the obvious reason that the X-ray fluorescence yield is extremely low for elements such as Li or Be. The EDS measurements can be used to qualitatively discuss the structural and chemical quality of $LiFe_{1.5}P_2O_7$. The respective peaks due to Fe, P, and O are indicated along with their respective energy positions. The lines identified are O Kα_1, P Kα, Fe Kα, Fe Kβ, Fe Lα, and Fe Lβ, respectively. The presence of peaks due to other elements either as dopants or impurities is not detected, which is an indication of the sample chemical purity. The elemental mapping images shown (Figure 5; lower panel) for $LiFe_{1.5}P_2O_7$ are of the representative particle used to analyze the elemental mapping of the respective elements. These images are uniform showing that the characteristic X-rays emit from Fe, P, and O simultaneously from the same location of point

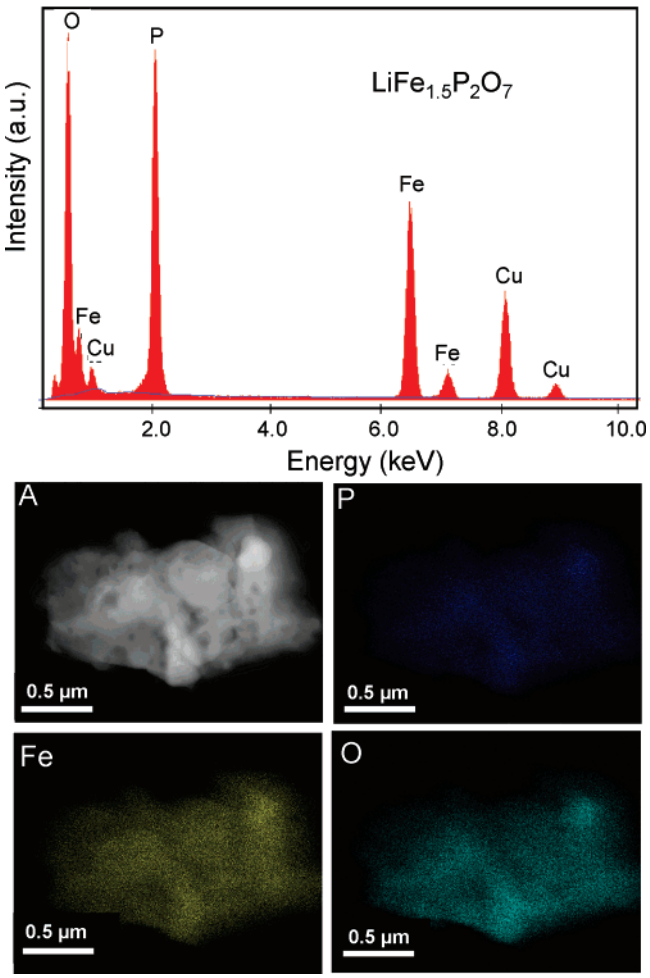

Figure 5. Upper panel: EDS spectrum of $LiFe_{1.5}P_2O_7$ grown by wet-chemical method. The spectrum exhibits the characteristic peaks of Fe, P, and O present in the sample. Lower panel: HAADF-STEM image of $LiFe_{1.5}P_2O_7$. The images labeled Fe, P, and O represent the elemental mapping of the respective elements.

and region, which is indicative of the chemical homogeneity of $LiFe_{1.5}P_2O_7$.

The magnetic studies (not shown here) indicate that $LiFe_{1.5}P_2O_7$ is a antiferromagnetic material with a Curie constant $C_p = 3.38$ emu K/mol per iron ion and a negative value of the Weiss temperature ($\Theta = -15$ K). The transition from the paramagnetic behavior that follows the Curie–Weiss law to the antiferromagnetic ordering appears at $T_N = 20$ K. Both zero-field cooled and field-cooled $\chi(T)$ curves are in good coincidence, and the linear plots of the isothermal magnetization curves $M(H)$ indicate the absence of Fe(III) impurities. The magnetic moment $\mu_{eff} = 5.20\ \mu_B$ is in good agreement with the structural model of spin-only for Fe^{2+} ions. Because the value of μ_{eff} is close to the spin-only value for Fe^{2+} in the high-spin configuration (4.9 μ_B). These results allow the following remarks: (i) the $LiFe_{1.5}P_2O_7$ framework does not contain Fe^{3+} impurities; (ii) the slight deviation of the magnetic moment is due to native defects in the pyrophosphate structure, that is, intrinsic Fe^{3+} ions associated with Li vacancies; (iii) similarly to most of the oxides the electronic features of $LiFe_{1.5}P_2O_7$ undergo an angular momentum $L = 0$ giving $\mu_{eff} = 2[S(S+1)]^{1/2}\ \mu_B$; and (iv) the low value of the Weiss constant ($\Theta = -15$ K), which indicates weak antiferromagnetic interactions, is due to the

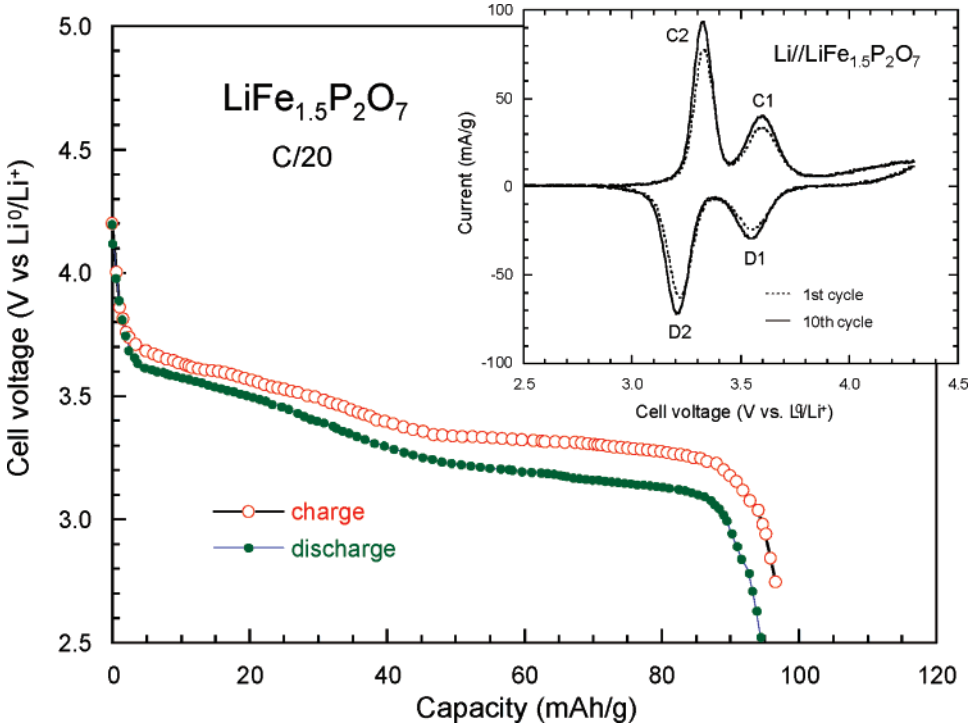

Figure 6. First charge−discharge profile for the Li/$LiPF_6$-EC-DEC/$LiFe_{1.5}P_2O_7$ cell with an electrode synthesized at 500 °C. Data were collected at the rate C/20 in the potential range 2.5−4.2 V. Insert shows the cyclic voltamogram recorded at a 0.1 mV/s sweep rate for the 1st and 10th charge−discharge cycle.

great distance between two equivalent magnetic ions that vanishes the Fe−O−Fe superexchange interactions.

B. Electrochemical Properties. Figure 6 displays the first charge−discharge profile of the Li//$LiFe_{1.5}P_2O_7$ cell which was cycled between 2.5 and 4.2 V at a C/20 rate. When the cell was charged up to 4.2 V, a reversible capacity 95 mA·h/g is obtained for a positive electrode with carbon additive (20 wt %). This value can be compared with the theoretical capacity of 101 mA·h/g for 1 e^- transferred. Both the charge and the discharge reaction for the Li//$LiFe_{1.5}P_2O_7$ cell occur with two steps displaying S-shaped curves. We can also remark that the good capacity retention is due to the thin carbon coating of the $LiFe_{1.5}P_2O_7$ particles that enhances considerably the electronic conduction between grains.

Cyclic voltammetry (CV) measurements (shown as an inset in Figure 6) present two sets of reduction and oxidation peaks, which are characteristics of the pyrophosphate structure with two nonequivalent iron sites. For the 1st and 10th cycles, the resulting CV curve indicates a totally reversible oxidation−reduction process that corresponds to a stable structure. The CV peaks are located at 3.33 and 3.60 V (charge) and at 3.56 and 3.22 V versus Li^0/Li^+ (discharge). The redox reaction appears to be highly reversible, and the CV peaks did not show any noticeable modification after 10 cycles.

Figure 7 shows the incremental capacity curves −(d*Q*/d*V*) versus cell voltage calculated from the charge−discharge profile shown in Figure 6. This graph displays the two sets of peaks that correspond to the extraction/insertion of Li^+ ions from/into the $LiFe_{1.5}P_2O_7$ host matrix, respectively. They are in good agreement with CV data. Each set is related to the two sites occupied by Fe ions that are energetically nonequivalent. As discussed previously, iron cations are located in octahedral sites with different spin configurations.

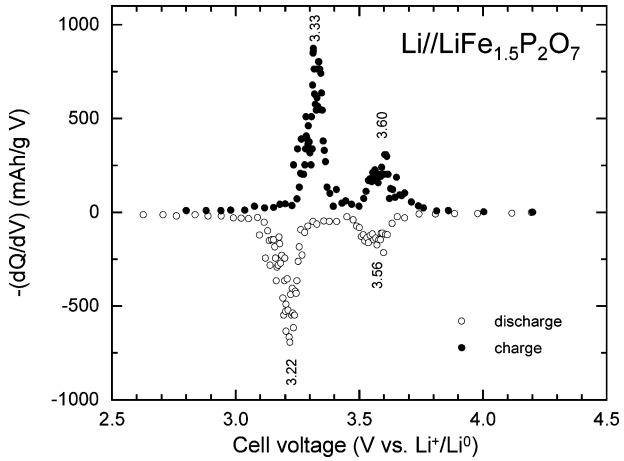

Figure 7. Incremental capacity vs potential for the Li//$LiFe_{1.5}P_2O_7$ cell. The −(d*Q*/d*V*) curves display the redox features during extraction (charge) and insertion (discharge) of Li ions from/into the $LiFe_{1.5}P_2O_7$ framework.

For the first cycle the resulting incremental capacity indicates a totally reversible oxidation−reduction process that corresponds to a stable structure. We observe any appearance of a sharp peak in the incremental capacity curves that could be the fingerprint of a voltage plateau for a two-phase system such as in $LiFePO_4$ or the occurrence of phase transition upon Li extraction.

The potential of the Fe^{2+}/Fe^{3+} couple is similar (3.60−3.33 V) in the Li//$LiFe_{1.5}P_2O_7$ couple and in the Li//$LiFePO_4$ couple (3.45 V) but higher than that in the Li//$LiFeP_2O_7$ (2.90 V).[1,30,31] A possible reason could be the inductive effect which is more pronounced in the olivine and in the dilithium

(30) Franger, S.; Le Cras, F.; Bourbon, C.; Rouault, H. *J. Power Sources* **2003**, *119−121*, 252.
(31) Yang, S.; Song, Y.; Ngala, K.; Zavalij, P. Y.; Whittingham, M. S. *J. Power Sources* **2003**, *119−121*, 239.

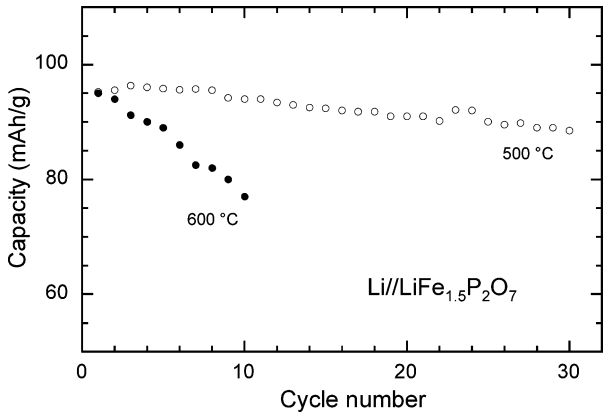

Figure 8. Plots of the capacity retention against cycle number for the Li//$LiFe_{1.5}P_2O_7$ cells with positive electrode synthesized at 500 and 600 °C. Cycling was carried out galvanostatically at constant charge−discharge current density of 0.5 mA/cm^2 between 2.5 and 4.2 V.

tri-iron bis(diphosphate) lattice than for the di-phosphate framework. As the inductive effect is related to the strong covalent bonding within the polyanion, the lowering of the Fe^{2+}/Fe^{3+} couple gives the higher potential versus Li^0/Li^+ for that couple. The correlation of the redox potential and the chemical bonding has been estimated for polyanionic compounds.[8] Because the vibrational features are sensitive to the covalency of phosphate group, an empirical relationship has been established between the covalency bonding factor and cell voltage for several lithium metal phosphates built by PO_4^{3-} and $P_2O_7^{4-}$ oxo-anions.

The plots of the capacity retention against cycle number for the Li//$LiFe_{1.5}P_2O_7$ cells with $LiFe_{1.5}P_2O_7$ positive electrode synthesized at 500 and 600 °C are shown in Figure 8. Cycling was carried out galvanostatically at constant charge−discharge current density of 0.5 mA/cm^2 between 2.5 and 4.2 V. The capacity for cathode material prepared at 500 °C slightly decreases with respect to cycle number at the rate of 0.22% per cycle while the capacity is falling rapidly in the case of a cathode material synthesized at 600 °C, which is attributed to the difference in microstructure of the materials.

IV. Summary and Conclusions

$LiFe_{1.5}P_2O_7$ has been successfully synthesized by wet chemistry from iron acetate raw material. Characterization of the microstructure of $LiFe_{1.5}P_2O_7$ powders has been performed using XRD, SAED, and HRTEM. Crystallographic studies have shown that $LiFe_{1.5}P_2O_7$ crystallizes in the monoclinic structure ($P2_1/c$ space group). Spectroscopic and chemical imaging analysis using EDS and HAADF-STEM indicates the high chemical quality of the grown samples. The lattice fringes observed in the HRTEM image indicate that the material is crystallized without lattice defects such as dislocations and misfits. The application of the grown $LiFe_{1.5}P_2O_7$ material in battery technology has been experimentally demonstrated using the electrochemical measurements carried out in lithium cells with nonaqueous electrolyte at 25 °C. The resulting charge−discharge profiles indicate a stable structure for the first cycle with potential of the redox peaks at 3.33 and 3.22 V versus Li^0/Li^+. The capacity for cathode material prepared at 500 °C slightly decreases with respect to cycle number at the rate of 0.22% per cycle while the capacity is falling rapidly in the case of a cathode material synthesized at 600 °C, which is indicative of the fact that the controlled microstructure of the material is important for employing these materials in electrochemical cells.

Acknowledgment. The authors thank M. Selmane for his assistance in XRD experiments.

CM071526M